http://dx.doi.org/10.1016/j.msea.2020.139939

Experimental investigations and constitutive modeling of the dynamic recrystallization behavior of Inconel 740 superalloy

Mingjia Wang[a,b], Chaoyang Sun[a,b,*], M. W. Fu[c,#], Zhongli Liu[d], Chunhui Wang[a,b]

[a] School of Mechanical Engineering, University of Science and Technology Beijing, Beijing, 100083, China

[b] Beijing Key Laboratory of Lightweight Metal Forming, Beijing, 100083, China

[c] Department of Mechanical Engineering, The Hong Kong Polytechnic University, Hung Hom, Kowloon, Hong Kong, China

[d] School of Nuclear Equipment and Nuclear Engineering, Yantai University, Yantai, 264005, China

Abstract

The dynamic recrystallization (DRX) behavior of Inconel 740 superalloy was investigated via the isothermal compression tests and constitutive model. The unified constitutive model involving the flow behavior and the microstructural evolution was proposed for modelling the DRX behavior through considering the critical strain of DRX initiation, DRX grain nucleation rate and DRX grain size. The results show that the variations of flow stress, grain size and DRX fraction during hot deformation are well described by the model at the constant strain rate. The strain hardening behavior is also well predicted under the deformation conditions outside the calibration range of this model. Moreover, the complex hot deformation characteristics covering stress and microstructure in the transient deformation process caused by the strain rate jump are also well predicted and estimated by this physical-based model. Furthermore, the DRX diagram in the optimum hot-workability temperature range of Inconel 740 superalloy is established to visualize the DRX kinetics. This work provides a basis for understanding the flow behavior and microstructural evolution of Inconel 740 superalloy in the hot forming process.

Keywords: Dynamic recrystallization; Hot deformation behavior; Constitutive model;

Dynamic recrystallization diagram; Inconel 740 superalloy

Corresponding authors:

* Chaoyang Sun: Tel.: +86-10-62332261, E-mail: suncy@ustb.edu.cn (C. Sun).

M. W. Fu: Tel.:852-27665572, Email: mmmwfu@polyu.edu.hk (M. W. Fu).

1. Introduction

Inconel 740 superalloy with its unique performance is promising to be used to make superheater and reheater pipes, and the tube material for advanced ultra-supercritical steam boiler unit [1, 2]. To promote its wide application in industries, huge efforts have been provided to study its creep behavior [3], thermal stability [4, 5] and oxidation behavior [6]. Moreover, Inconel 740 superalloy similar to other Nickel-based superalloys with the low stacking fault energy (SFE), since the dynamic recovery (DRV) is retarded by reason of the dissociation reaction impeding the climb and cross slip of dislocation [7], the dynamic recrystallization (DRX) can be considered as the preponderant softening mechanism in its hot deformation process. The DRX mechanisms of Inconel 740 superalloy during hot deformation were specifically demonstrated in our recent report [8]. However, there is less focus on the development of constitutive model, which is indispensable for predicting and modeling the DRX behavior of this superalloy. Meanwhile, the numerical simulation during hot forming is based on the applicable constitutive modeling. How to establish the applicatory model to accurately predict the flow behavior and microstructure evolution of Inconel 740 superalloy is critical.

From the microstructure-property aspect, the desirable properties of metallic material components are fully dependent on the reasonable microstructure. The forming process parameters, including strain rate, strain and deformation temperature, in hot forming process can make a significant difference to the microstructure evolution. The more applicable constitutive modelling should include microstructure evolution involved in the deformation process. Many constitutive models involving Arrhenius, Zerilli-Armstrong, and Johnson-Cook models [9-11], were developed to estimate the flow stress of metallic materials. Meanwhile, the microstructure evolution (DRX volume fraction) during hot deformation of metallic materials was described by Avrami equation [12]. The above models are the empirical and phenomenological description in nature. They do not consider the influence of physical mechanisms related to the dislocation on the behavior of hot deformation. The dislocation density as an important factor has a great impact on the flow and

microstructure characteristics during thermoplastic deformation of materials. The physically-based constitutive model correlating the dislocation mechanics caused by work hardening, DRX and DRV can better represent the constitutive behavior of metallic materials. With the help of physically-based constitutive models, the flow behaviors of duplex stainless steel [13], aluminium alloy [14], nickel-based superalloy [15] and medium carbon and vanadium microalloyed steels [16] had been well predicted and verified. These models, however, do not model the dependence of microstructure evolution on dislocation density in a unified way. In tandem with this, Lin et al. [17] depicted the variations of flow stress, grain size and recrystallization fraction during hot forming of a micro-alloyed steel through the proposed physically-based unified viscoplastic constitutive model. According to the framework of this model, Ji et al. [18] set up the unified constitutive model to display the true stress, grain size and DRX volume fraction during hot deformation of 5Cr21Mn9Ni4N steel, but they did not consider the evolution of DRX grain size and did not also conduct the experimental verification of DRX fraction in the model. Su et al. [19] developed a unified constitutive model without considering grain size evolution for predicting the true stress and DRX volume fraction during hot deformation of AZ80 magnesium alloy. Xiao et al. [20] performed the constitutive modeling without taking into account the recrystallization behavior of AA7075 aluminum alloy under hot stretching conditions, and the predicted data agreed with the experimental stress and grain size. These above researches have been revealed that to some extent, the hot deformation behavior of metal materials could be well evaluated and predicted by those unified constitutive models. However, the above several models were a bit imperfect for predicting the DRX behavior of metallic materials. Therefore, a more rigorous constitutive model predicting DRX behavior of materials which are prone to the occurrence of DRX should be developed.

In the current study, for Inconel 740 superalloy, a physically-based unified constitutive model considering the flow stress, grain size and DRX fraction during hot deformation was developed under the framework of Lin et al [17, 21]. The hot deformation characteristics during the plastic forming of Inconel 740 superalloy were

reasonably described by introducing the critical strain of DRX initiation, DRX grain nucleation rate and DRX grain size into the constitutive model. The applicability of this model was verified by the transient deformation caused by the change of strain rate during hot deformation. Furthermore, the optimal hot-workability window of Inconel 740 superalloy was presented by Wang et al. [22]. Based on the proposed model, the DRX diagram was finally established to represent the DRX kinetics in the optimum hot-workability temperature range of the superalloy.

2. Experimental procedure

The material studied is Inconel 740 superalloy with a nominal composition (*wt*.%) of 0.03C-0.5Mo-0.5Si-0.3Mn-20Co-0.9Al-25Cr-0.7Fe-1.8Ti-2.0Nb and (Bal.) Ni. The specimens of φ 8×12mm taken from a forged billet were annealed at 1150 ˚C for 30 min, and subsequently water-cooled. A series of hot compression tests were implemented on Gleeble-3500 thermal simulator. Before loading, these specimens were heated with a rate of 5 ˚C/s to the presupposed temperature, and subsequently soaked for 3 min. Based on the fact that DRX behavior depending on the different strain rates and deformation temperatures, Fig. 1 (a) showed the experimental plans with the constant strain rate. The microstructures at the four true strain of 0.22, 0.36, 0.51 and 0.8 in Fig. 1 (a) were observed, respectively. Furthermore, in the transient deformation process, the deformation temperature was always 1100 ˚C and Fig. 1 (b) sketched the two cases of strain rate jump. In case I, the strain rate of 0.01 s^{-1} was used before the true strain of 0.36, while the strain rate of 0.1 s^{-1} was performed after that. By comparing with case I, the imposed strain rate was sequentially exchanged in case II. In these two cases, the microstructures at the true strains of 0.51 and 0.8 were obtained. After the load stopping, the high temperature microstructure of compressed specimen was frozen by water quenching.

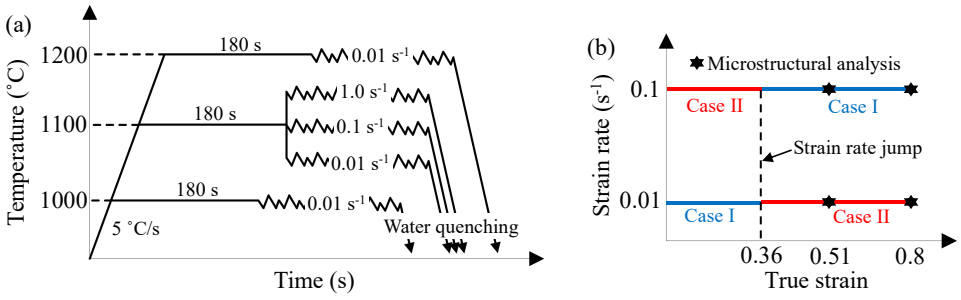

Fig.1. Schematic of isothermal compression tests of Inconel 740 superalloy: (a)

constant strain rate and (b) two cases of the transient deformation.

These compressed specimens were sectioned longitudinally for analysis of their microstructures and the location of microstructural observation was in the center area of above sections. These observation surfaces were electropolished for 12 s in a mixture of 40 ml vitriol and 160 ml methyl alcohol at room temperature after being ground and mechanically polished. In analysis of electron back-scatter diffraction (EBSD), the area of more than 1 mm^2 was scanned to give a statistically reliable representation for evaluating the average grain size (AGS) and DRX fraction. The scanning step size in the performance process of EBSD was 1.8 μm. The scanned data were processed subsequently through the software Channel 5. The equivalent grain size and DRX fraction in the scanned area were automatically measured through this software. In particular, according to the literatures [23, 24], with the help of the grain reconstruction function in Tango module of Channel 5, the fraction of DRX grains was estimated via measuring the average misorientation angle of grain interiors. Moreover, the microstructure of Inconel 740 superalloy was represented through the inverse pole figure (IPF) map. A grain in IPF map was identified as a region surrounded by the grain boundaries (the black lines) whose misorientation angle was larger than 15° [25]. Specially, the AGS valuation included the annealing twin boundaries [26, 27].

3. Experimental results under the constant strain rate

3.1. Initial microstructure

The microstructure after annealing treatment and before hot deformation is defined as the initial state of Inconel 740 superalloy. Fig. 2 shows the microstructure and grain size distribution of initial state. From Fig. 2 (a), the near-equiaxial static recrystallized (SRX) grains are observed. The color codes of grain orientation are the same as the following IPF maps. The abundant annealing twins with the misorientation angle larger than 15° in the equiaxed grains and some small SRX grains result in the non-uniform grain size distribution in Fig. 2 (b). It is apparent that the grain size distribution of initial material mainly locates in the range of smaller than 200 μm and the initial AGS is identified as 58.5 μm.

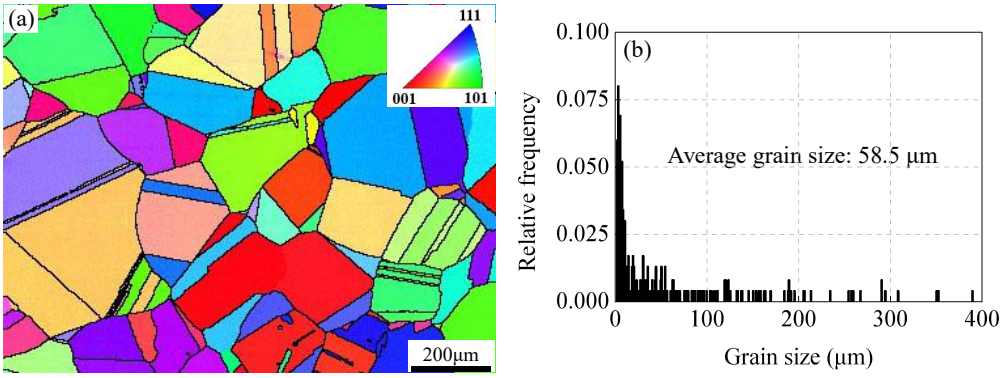

Fig.2. The initial state of Inconel 740 superalloy: (a) microstructure and (b) grain size distribution.

3.2. Effect of strain rate on microstructure

Fig. 3 illustrates the influence of different strain rates on the microstructure evolution of Inconel 740 superalloy. The fraction and size of DRX grains are significantly decreased with the increase of strain rate. Commonly, the higher strain rate provides the greater dislocation density used for DRX grain nuclei [28]. However, the insufficient deformation time resulting from the higher strain rate impedes the formation and growth of the nuclei of DRX grains. Furthermore, the plentiful bulging and serrated original boundaries are always observed in Fig. 3. The position of these serrated boundaries is regarded as the potential nucleation sites of new grains during subsequent hot deformation [29]. Most of DRX grains are generated at the initial boundaries and arranged in a necklace structure. The microstructural characteristics demonstrate the DRX grain nucleation resulting from the bulging of the original grain boundaries [8, 30, 31]. On the other hand, as illustrated by the rectangle in Fig. 3 (b), a new grain is formed by the subgrain evolution [8]. This subgrain orientation is different from the parent grain and its boundary is transformed into a grain boundary whose the misorientation angle is larger than 15°. Moreover, from Fig. 3, some new grain shown by the arrows appear in the deformed grain interiors. These DRX grains are produced by the progressive subgrain rotation [8, 31]. The typical microstructural characteristic during hot deformation of Inconel 740 superalloy, i.e., the generation of DRX grains within the initial grains, is similar to other Nickel-based superalloys [12,

32, 33].

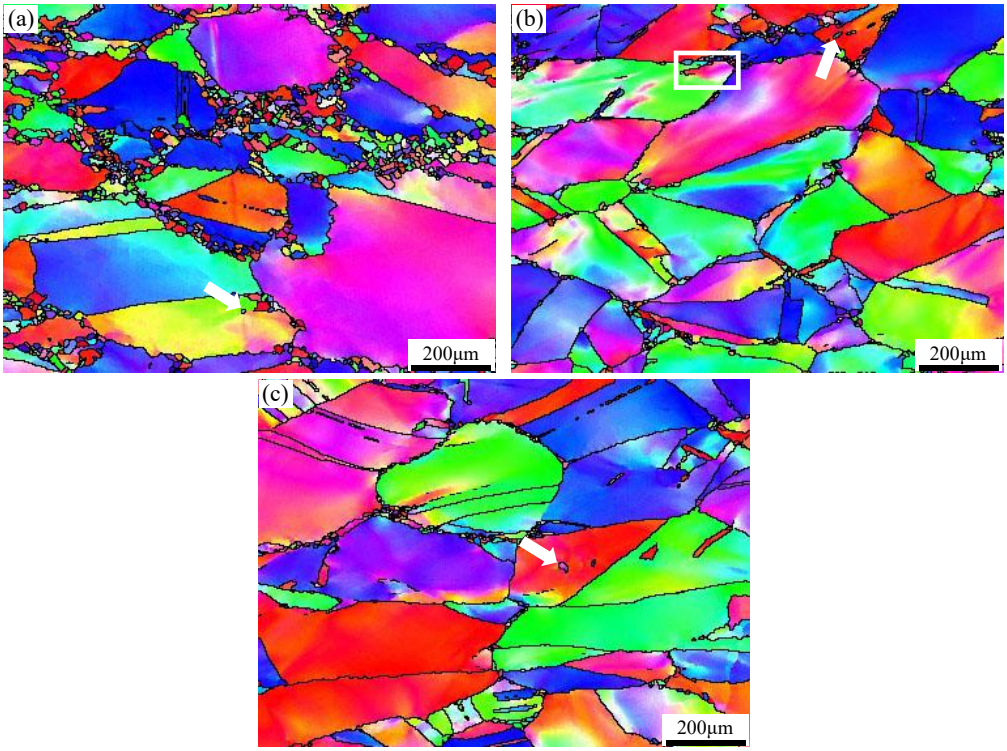

Fig.3. The microstructure of Inconel 740 superalloy obtained at the true strain of 0.36 and 1100 ˚C with a strain rate of (a) 0.01 s^{-1}, (b) 0.1 s^{-1} and (c) 1.0 s^{-1}.

3.3. Effect of deformation temperature on microstructure

Fig. 4 displays the microstructures of Inconel 740 superalloy at different deformation temperature and 0.01 s^{-1}. Apparently, the fraction and size of DRX grains are increased with deformation temperature. The sufficient driven force used for the migration of grain boundaries is increased through the incremental deformation temperature, which promotes the development of DRX grains. When the temperature is 1000 ˚C, as shown in Fig. 4 (a), only a few DRX grains are formed at the initial grain boundaries and the triangular junctions. Fig. 4 (b) illustrates that the more DRX grains appear in the microstructure obtained at 1100 ˚C. The necklace-like structures made up of DRX grains exhibit along the original grain boundaries. Furthermore, some DRX grains are also formed at the initial twin boundary, as shown by the rectangular area in Fig. 4 (b). The initial twin boundaries lose their twinning nature due to dislocation accumulation [34]. They are transformed into the usual grain boundaries with the misorientation angle greater than 15° during hot deformation.

Therefore, the nucleation of DRX grains at the initial twin boundaries should be more deferred than that at the initial grain boundaries. Fig. 4 (c) illustrates that the original deformed grains almost disappear while the near-equiaxed DRX grains are dominant in the microstructure obtained at 1200 ˚C. Moreover, form Fig. 4, the generation of DRX grains shown by the arrows within the initial grains indicates the role of the subgrain evolution.

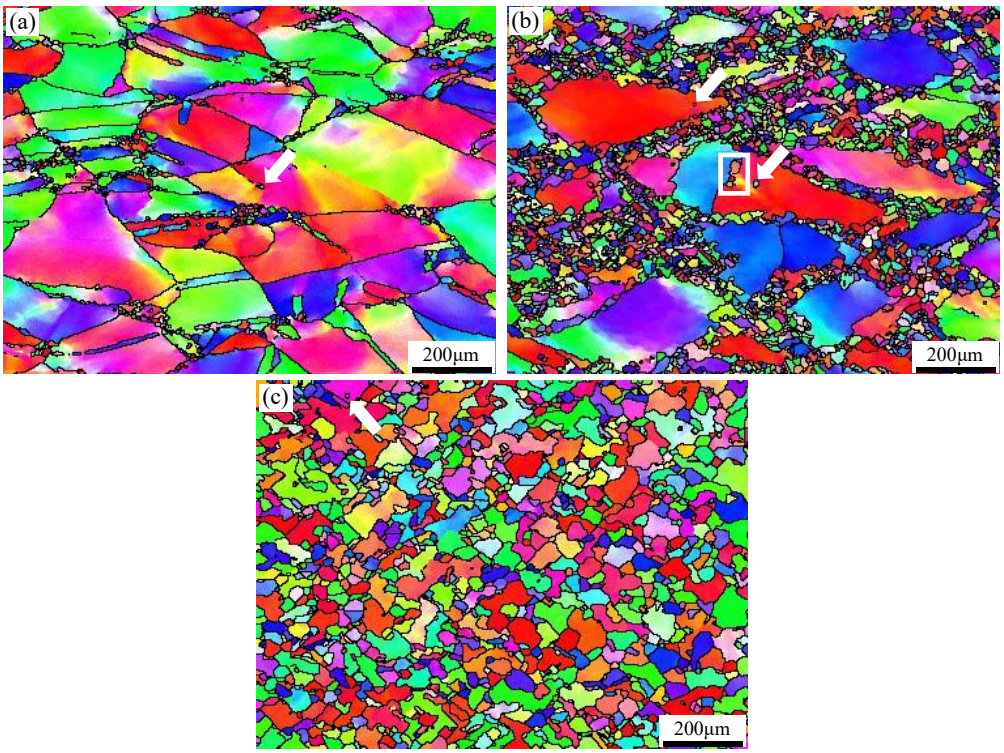

Fig.4. The microstructure of Inconel 740 superalloy obtained at the strain of 0.51 and 0.01 s^{-1} with a deformation temperature of (a) 1000 ˚C, (b) 1100 ˚C and (c) 1200 ˚C.

3.4. Effect of strain on microstructure

Under the strain rate of 0.01 s^{-1} and the deformation temperature of 1200 ˚C, the microstructures of Inconel 740 superalloy at different true strains are displayed in Fig. 5. The DRX fraction is significantly increased with strain, since the higher deformation stored energy from the higher true strain provides the greater driven force for the grain boundary migration. Fig. 5 (a) and (b) demonstrate that there are the necklace-like structures consisting of several layers of DRX grains between the initial grains at the true strain of 0.22 and 0.36, respectively. With the increase of strain to

0.8, Fig. 5 (c) shows the full DRX microstructure. Moreover, by comparing the microstructures of the strains of 0.51 and 0.8 given in Figs. 4 (c) and 5 (c), the growth of DRX grains is clearly observed. Furthermore, through the progressive subgrain rotation, some new grains shown by the arrows form in the grain interiors, as shown in Fig. 5.

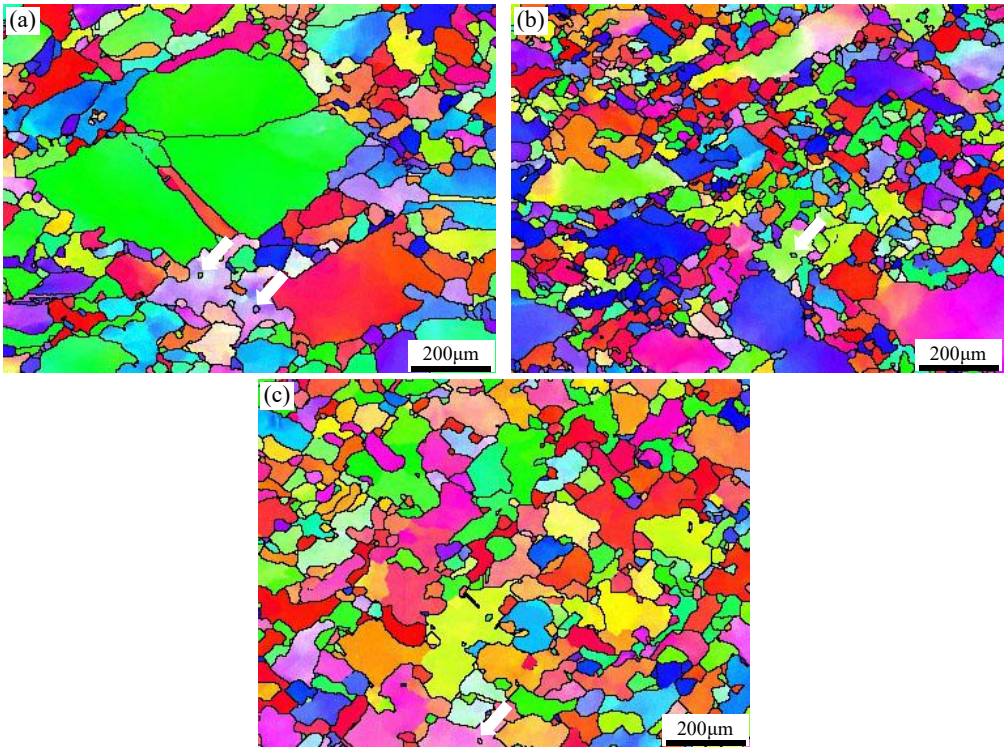

Fig.5. The microstructure of Inconel 740 superalloy obtained at 0.01 s^{-1} and 1200 ˚C with a true strain of (a) 0.22, (b) 0.36 and (c) 0.8.

4. Unified constitutive modeling

4.1. Flow rule

A relationship of stress and strain during deformation is described by the flow rule of materials. The total strain can be composed of elastic (reversible) and the plastic (irreversible) strains. The flow stress σ is given through Hooke's law [21, 35]:

$$\sigma = E(\varepsilon_t - \varepsilon_p) \tag{1}$$

where ε_t and ε_p are the total strain and plastic strains, respectively. E is Young's modulus and its values of different temperatures can be obtained by JMatPro

software.

In Eq. (2), the total flow stress can be made up of hardening stress H, initial yield stress k and viscoplastic stress σ_v during hot deformation process.

$$\sigma = H + k + \sigma_v \tag{2}$$

During hot deformation of metallic materials, the hyperbolic sine law in Arrhenius equation applied to the large-scale stress and strain levels is more suitable for expressing the flow stress [36]. The preliminary flow rule is represented as follows:

$$\dot{\varepsilon}_p = A_1 \sinh[A_2(\sigma - H - k)] \tag{3}$$

where A_1 is a temperature-dependent variable and the change of k value is related to temperature, A_2 is a material constant, $\dot{\varepsilon}_p$ represents the plastic strain rate.

H in Eq. (3) is connection with the dislocation evolution. Therefore, the isotropic hardening rate $\dot{H}$ is defined as [37-39]:

$$\dot{H} = 0.5B\bar{\rho}^{-0.5}\dot{\bar{\rho}} \tag{4}$$

where B represents a temperature-dependent variable and expresses the impact of dislocation density on the material hardening, ρ is the dislocation density and will be discussed in the following section.

Furthermore, the grain size evolution has an effective impact on the flow behavior for metallic materials. Hence, the grain size term is coupled into Eq. (3). Finally, the flow rule expression is given as:

$$\dot{\varepsilon}_p = A_1 \sinh[A_2(\sigma - H - k)](d/d_0)^{-\gamma_1} \tag{5}$$

where γ_1 is a material constant and represents the influence of AGS on the viscoplastic flow behavior, d is AGS and discussed in the later sections, d_0 represents the initial grain size.

4.2. Microstructural model

4.2.1. Dislocation density modeling

The measurement and evaluation of absolute dislocation density are not easy to implement during hot deformation of metallic materials. An expression of normalized

dislocation density $\bar{\rho}$ is thus introduced and denoted as:

$$\bar{\rho}=1-\rho_0/\rho \tag{6}$$

where ρ_0 and ρ indicate the dislocation densities of the initial and deformed materials, respectively. The value of $\bar{\rho}$ ranges from 0 to 1. Based on the relevant thermoplastic deformation mechanisms of the superalloy, the normalized dislocation density rate $\dot{\bar{\rho}}$ is given by Eq. (7) [20, 21]:

$$\dot{\bar{\rho}}=A_4(d/d_0)^{\delta_1}(1-\bar{\rho})|\dot{\varepsilon}_p|^{\delta_2}-C_1\bar{\rho}^{\delta_3}-\dot{X}[(A_3\bar{\rho})/(1-X)^{\delta_4}] \tag{7}$$

where C_1 is a temperature-dependent variable, A_3, A_4, δ_1, δ_2, δ_3 and δ_4 are material constants, X is the DRX fraction and will be discussed in the following section. C_1 characterizes the combined effects of the average energy per unit length of a dislocation and the grain boundary mobility, and A_4 has an impact on the slope of the hardening curve.

The two mechanisms are in connection with the dislocation density evolution of metallic materials during hot deformation. One is the dislocation multiplication from the work hardening. The dislocation annihilation caused by the recovery and recrystallization processes is regarded as the other one. The dislocation density accumulation from the plastic deformation is represented by the first term in Eq. (7). Moreover, the role of grain size is also introduced into this term. The larger AGS during hot deformation results in the smaller degrees of grain rotation and grain boundary sliding, increasing the dislocation density. Furthermore, the second and third terms in Eq. (7) represent the dislocation density evolution involved in the recovery and recrystallization, respectively.

4.2.2. Determination of dynamic recrystallization fraction

For Inconel 740 superalloy with low SFE, the DRX behavior takes place as long as the critical strain (ε_c) of DRX initiating is reached. ε_c is determined correspondingly based on the critical stress (σ_c) value of DRX initiating on the true stress-strain curve. σ_c at 0.01 s^{-1} and 1100 ˚C is acquired through the inflection point abscissa on stress (σ)-strain hardening rate ($\theta=d\sigma/d\varepsilon$) curve [40, 41], as shown in the small diagram of

Fig.6 (a). In addition, Zener-Hollomon (Z) parameter can be as following:

$$Z = \dot{\varepsilon} \exp\left(Q/RT\right) \tag{8}$$

where T is the deformation temperature (K), Q represents the activation energy of hot deformation (kJ/mol), $\dot{\varepsilon}$ represents the strain rate (s^{-1}).

For Inconel 740 superalloy, the value of Q is 373.86 kJ/mol [22]. The function of ε_c and Z parameter is expressed as [42]: $\varepsilon_c = D_1 Z^{m_1}$, where D_1 and m_1 are material constants. For making this power-law function more statistical and reliable, ε_c values of Inconel 740 superalloy at the strain rate of 0.01, 0.1 and 1.0 s^{-1} and temperature of 1000, 1100 and 1200 ˚C are displayed in Fig. 6 (a). The experimental results of these deformation conditions are obtained by the analysis of the flow stress from the study [22]. Therefore, through the linear fitting in Fig. 6 (b), the function between ε_c and Z parameter is given as:

$$\varepsilon_c = 0.002314 Z^{0.13398} \tag{9}$$

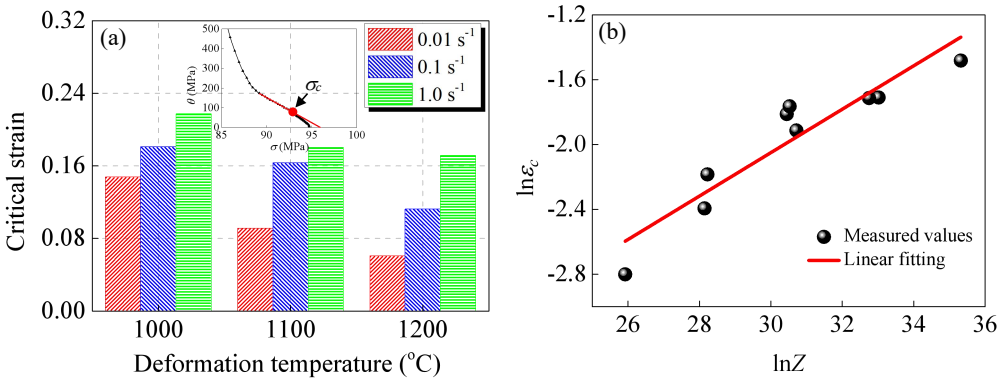

Fig.6. The critical strain of Inconel 740 superalloy: (a) the ε_c values and the example of determination of σ_c value and (b) the relationship between ε_c value and Z parameter.

The DRX fraction depends on the new grain nucleation and growth, which are relevant to the evolution of dislocation density. The grain size evolution will be discussed in the next section. The nucleation rate of DRX grains is related to strain rate and deformation temperature [43-45] and is designated as:

$$\dot{n}\left(\dot{\varepsilon},T\right)=N_0\dot{\varepsilon}^b\exp\left(-Q_n/RT\right) \tag{10}$$

where N_0 and b represent material constants, Q_n is activation energy.

On the basis of the literature [18], by coupling the nucleation rate of DRX grains, normalized dislocation density and critical strain of initiating DRX, the DRX volume fraction X is proposed by Eq. (11):

$$\dot{X}=\overline{\rho}[x\varepsilon-\varepsilon_c(1-X)](1-X)^{\lambda_1}N\dot{\varepsilon}_p^b \tag{11}$$

where λ_1 and b represent material constants, $N\dot{\varepsilon}_p^b$ term represents the right side of Eq. (10) and N is a temperature-dependent variable, $\dot{X}$ represents DRX fraction rate.

The occurrence of DRX behavior requires an incubation period. The parameter x in Eq. (11) can describe this phenomenon and the incubation fraction x is expressed as [38]:

$$\dot{x}=A_0(1-x)\overline{\rho} \tag{12}$$

where A_0 is a temperature-dependent variable. The value of x varies from 0 to 1 and $\dot{x}$ is the incubation fraction rate.

4.2.3. Determination of grain size

The fact that both the growth and refinement of grains take place concurrently is undoubted in the thermoplastic deformation process. The DRX occurrence after ε_c causes grain refinement in microstructure. The AGS evolution is as the result of the competition between the growth and refinement of grains [46]. The migration rate of grain boundaries can be affected by thermal effect. The grain growth is correlated with the migration of grain boundaries, which is regarded as the atomic diffuse process. The grain growth rate $\dot{d}_g$ can be expressed through Eq. (13) [17, 20].

$$\dot{d}_g=M\sigma_{surf}d^{-\gamma_0} \tag{13}$$

where γ_0 is a material constant, M represents the mobility of grain boundaries, σ_{surf} is the energy density of grain boundaries. Eq. (13) is re-designated as:

$$\dot{d}_g=G_1\left(d_1/d\right)^{\varphi_1} \tag{14}$$

where G_1 is a temperature-dependent variable representing $M\sigma_{surf}$ term in Eq. (13);

d_1 and φ_1 are material constants.

Based on the literatures [18, 40, 47], by coupling DRX grain size, the grain refining rate ($\dot{d}_r$) caused by the recrystallization behavior is re-expressed as:

$$\dot{d}_r = -G_2 \dot{X}^{\lambda_2} (d/d_d)^{\varphi_2} \tag{15}$$

where G_2 is a temperature-dependent variable, φ_2 and λ_2 are material constants, d_d represents DRX grain size.

With the DRX occurrence, AGS is decreased by reason of the increase of total grain number. By combining Eqs. (14) and (15), the AGS rate is formulated as:

$$\dot{d} = G_1 (d_1/d)^{\varphi_1} - G_2 \dot{X}^{\lambda_2} (d/d_d)^{\varphi_2} \tag{16}$$

The power-law function between DRX grain size (d_d) in Eq. (16) and Z parameter is expressed as [48]: $d_d = D_2 Z^{m_2}$, where D_2 and m_2 are material constants. For obtaining the statistical and reliable function, the deformation condition for the obtainment of DRX grain sizes is the same as that of ε_c in Section 4.2.2. The DRX grain sizes of different deformation conditions are acquired through the linear intercept method of metallography from the report [22] and are illustrated in Fig. 7 (a). Therefore, through the linear fitting in Fig. 7 (b), the function between Z parameter and d_d is given as:

$$d_d = 13146.226 Z^{-0.23535} \tag{17}$$

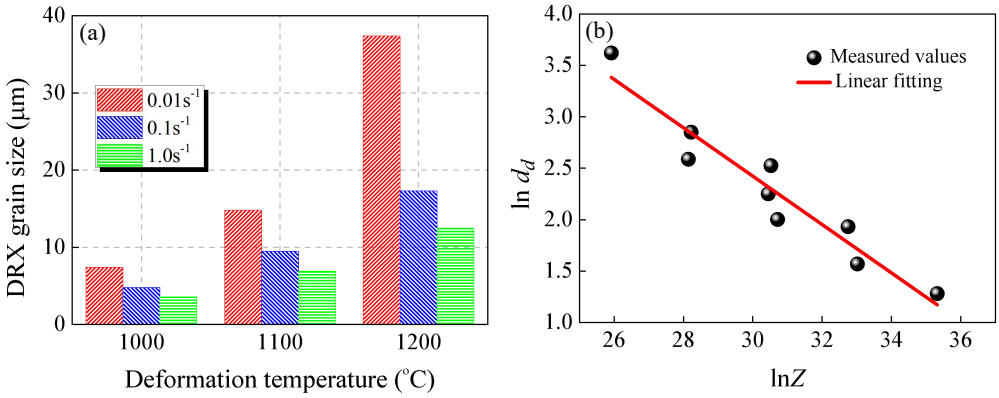

Fig.7. The DRX grain size of Inconel 740 superallly: (a) the d_d values and (b) the relationship between d_d and Z parameter.

4.3. Formulation of the unified constitutive model

The unified viscoplastic constitutive model is developed for modelling the evolutions of strain hardening, fraction and size of DRX grains and dislocation density, and rationalizing the influence of these evolutions on the plastic flow behavior and their inherent relationships during hot deformation of Inconel 740 superalloy. The group of unified constitutive equations can be formulated below and the superscript '·' implies the change rate of the physical parameters with time.

$$\begin{cases} \dot{\varepsilon}_p = A_1 \sinh[A_2(\sigma - H - k)](d/d_0)^{-\gamma_1} \\ \dot{H} = 0.5B\overline{\rho}^{-0.5}\dot{\overline{\rho}} \\ \dot{\overline{\rho}} = A_4(d/d_0)^{\delta_1}(1-\overline{\rho})\,|\,\dot{\varepsilon}_p\,|^{\delta_2} - C_1\overline{\rho}^{\delta_3} - \dot{X}[(A_3\overline{\rho})/(1-X)^{\delta_4}] \\ \dot{X} = \overline{\rho}[x\varepsilon_T - \varepsilon_c(1-X)](1-X)^{\lambda_1} N\dot{\varepsilon}_p^b \\ \dot{x} = A_0(1-x)\overline{\rho} \\ \dot{d} = G_1(d_1/d)^{\varphi_1} - G_2\dot{X}^{\lambda_2}(d/d_d)^{\varphi_2} \\ \sigma = E(\varepsilon_T - \varepsilon_p) \end{cases} \tag{18}$$

where A_1, k, B, C_1, N, A_0, G_1 and G_2 are the temperature-dependent variables and they can be written as the classic temperature compensation parameters in the following Arrhenius-type equations:

$$\begin{cases} A_1 = A_{10}\exp(-Q_{A1}/RT) \\ k = k_0\exp(Q_k/RT) \\ B = B_0\exp(Q_B/RT) \\ C_1 = C_{10}\exp(-Q_{c1}/RT) \\ N = N_0\exp(-Q_N/RT) \\ A_0 = A_{00}\exp(-Q_{A0}/RT) \\ G_1 = G_{10}\exp(-Q_{G1}/RT) \\ G_2 = G_{20}\exp(-Q_{G2}/RT) \end{cases} \tag{19}$$

where A_{10}, k_0, B_0, C_{10}, N_0, A_{00}, G_{10} and G_{20} are material constants, respectively. Q_{A1}, Q_k, Q_B, Q_{C1}, Q_N, Q_{A0}, Q_{G1} and Q_{G2} are the activation energies corresponding to the temperature-dependent variables on the left side of Eq. (19), respectively. The value of R is 8.314 J·mol^{-1}·K^{-1}.

The unified viscoplastic constitutive model represented in Eq. (18) is a group of

highly coupled nonlinear differential equations. These material constants in Eqs. (18) and (19) can be determined by the optimization technique from the genetic algorithm in the software MATLAB. The optimization aims at minimizing the residuals between the computed data and experimental values. The experimental values used to optimize the material constant result from the plan in Fig. 1 (a). The optimization process is detailed elsewhere [17, 49-51]. Therefore, the repetitive description is unnecessary. Table 1 lists the above material constant values.

Table 1. The material constant values in the unified constitutive model of Inconel 740 superalloy.

Material constants	Optimum values	Material constants	Optimum values
k_0 (MPa)	2.301×10^{-2}	Q_k (J/mol)	8.750×10^{4}
A_{10} (--)	1.909×10^{12}	Q_{A1} (J/mol)	3.731×10^{5}
N_0 (--)	8.869×10^{4}	Q_{N0} (J/mol)	1.162×10^{5}
C_{10} (--)	6.244×10^{11}	Q_{C1} (J/mol)	2.963×10^{5}
A_{00} (--)	4.425×10^{5}	Q_{A0} (J/mol)	9.022×10^{4}
B_0 (MPa)	6.714	Q_{B0} (J/mol)	3.353×10^{4}
G_{10} (--)	4.036×10^{14}	Q_{G1} (J/mol)	3.521×10^{5}
G_{20} (--)	36.254	Q_{G2} (J/mol)	1.652×10^{4}
A_2 (--)	0.058	γ_1 (--)	0.263
λ_1 (--)	0.072	A_3 (--)	6.662
A_4 (--)	5.562	δ_1 (--)	0.031
δ_2 (--)	1.328	δ_3 (--)	2.149
δ_4 (--)	1.623	d_1 (--)	2.082
φ_1 (--)	1.873	b (--)	0.194
λ_2 (--)	0.623	φ_2 (--)	2.213

5. Results and discussion

5.1. The calculated results of the unified constitutive model

The comparisons of experimental and computed true stress under the different strain rates and temperatures are presented in Fig. 8 (a) and (b), respectively. The solid curves and symbols in Fig. 8 represent the computed data and experimental values, respectively. The calculated curves match well the experimental results of the corresponding deformation conditions. The characteristic of single peak stress is exhibited on these stress-strain curves, implying the anteroposterior two stages dominated by strain hardening and dynamic softening due to the dislocation multiplication and annihilation, respectively. Furthermore, with the increase of strain, Fig. 8 (a) shows that the predicted stress at 1100 ˚C and 10 s^{-1} also is in good agreement with the experimental result. The deformation condition is outside the calibration range, indicating the model with a well ability to predict the flow stress at high strain rate.

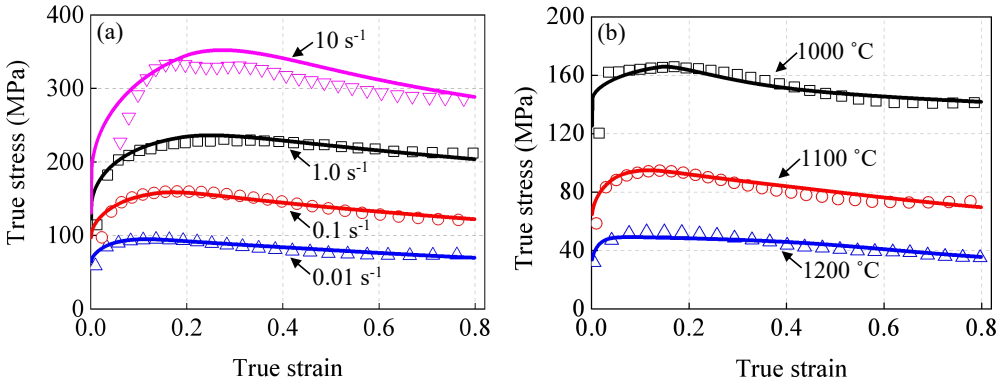

Fig.8. Comparison of calculated (solid curves) and experimental (symbols) true stress of Inconel 740 superalloy at (a) 1100 ˚C and (b) 0.01 s^{-1}.

Fig. 9 shows the calculated curves and experimental values for the microstructure evolution, including AGS and DRX fraction. The solid curves and the symbols represent the calculated data and the experimental values, respectively. Fig. 9 (a) and (b) give the variations of AGS and DRX fraction at the different strain rates, respectively. When the plastic deformation reaches ε_c, as shown Fig. 9 (a), with the

occurrence of DRX, the AGS curves are observably decreased, while the downward trend at 0.01 s^{-1} is more obvious. The low strain rate more benefits the DRX initiation and increases the total number of grains. Under the large deformation condition, the calculated curve at 0.01 s^{-1} is increased slightly, and AGS can be considered to reach a steady state. However, the calculated curves are continuously decreased at 0.1 and 1.0 s^{-1}. The decreasing tendency at 1.0 s^{-1} is more apparent. Therefore, the high strain rate makes the grain refinement more significant at the large strain. Manonukul et al. [52] and Cram et al. [53] also reached the same conclusions. One of the reasons is the comprehensive effect of different DRX fractions and DRX grain sizes as a result of different strain rates. Both the size and fraction of DRX grains should be concurrently considered to correctly interpret the AGS evolution [46]. The other is that based on Derby's relation [54], the small AGS is generated by the high stress corresponding to the high strain rate. Furthermore, Fig. 9 (b) illustrates that the computed curve of DRX fraction is expectedly increased with the decrease of strain rate and the increase of strain.

Fig. 9 (c) and (d) reveal the variations of AGS and DRX fraction at the different deformation temperatures, respectively. From Fig. 9 (c), the decline of the calculated curve at 1100 ˚C is more prominent than that at 1000 ˚C and 1200 ˚C. The low temperature (1000 ˚C) leads to the limited number of DRX grains when the true strain reaches ε_c. Although the high temperature (1200 ˚C) increases the number of DRX grains, it also increases the DRX grain size. Therefore, compared with 1100 ˚C, the refinement of microstructures obtained at these two temperatures is less significant at the low strain. However, the low deformation temperature is more favourable to the grain refinement at the large strain. Moreover, from Fig. 9 (c), it appears that the computed curve at 1200 ˚C has an initial grain growth trend before ε_c. Two driving forces, including the stored deformation energy (SDE) and grain boundary energy (GBE), can promote the grain growth [46]. The initial state of Inconel 740 superalloy is fully annealed at 1150 ˚C and the microstructure consisting of SRX grains is illustrated in Fig. 2 (a). Thus, the initial state of material has the low stored energy since the SDE obtained from the as-received forging billet drives the SRX grain

growth [55]. When the specimen is heated again to the deformation temperature (1200 ˚C) above its annealing temperature (1150 ˚C), the initial SRX grain growth is driven by GBE resulting from the thermally activated mechanism due to the higher temperature and new SDE [56]. Moreover, the sufficient time for the grain growth is also provided by the low strain rate (0.01 s^{-1}). Therefore, the growth stage of initial grains forecasted by this unified constitutive model before ε_c at 1200 ˚C and 0.01 s^{-1} can be explained. Furthermore, Fig. 9 (d) reveals that the calculated curve of DRX fraction is increased with strain and temperature. In addition, in terms of visual display, as presented in Fig. 9, the experimental results of AGS and DRX fraction at the different strain rates and temperatures agree well with the corresponding calculated curve.

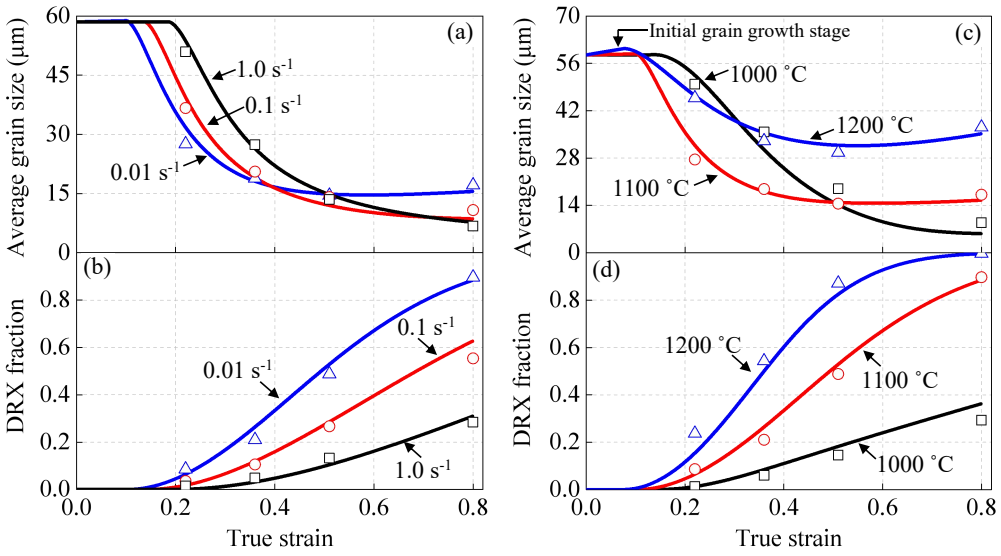

Fig.9. Comparison between the calculated (solid curves) and experimental (symbols) data of Inconel 740 superalloy for (a) AGS, (b) DRX fraction at 1100 ˚C and different strain rates and (c) AGS, (d) DRX fraction at 0.01 s^{-1} and different deformation temperatures, respectively.

Through some statistical parameters, the accuracy of the proposed model is quantitatively analyzed. These parameters, including the root mean square error (*RMSE*), correlation coefficient (*R*) and average absolute relative error (*AARE*) are

given in Eqs. (20)-(22), respectively.

$$RMSE = \sqrt{\frac{1}{N}\sum_{i=1}^{N}(E_i - C_i)^2} \tag{20}$$

$$R = \frac{\sum_{i=1}^{N}(E_i - \bar{E})(C_i - \bar{C})}{\sqrt{\sum_{i=1}^{N}(E_i - \bar{E})^2}\sqrt{\sum_{i=1}^{N}(C_i - \bar{C})^2}} \tag{21}$$

$$AARE = \frac{1}{N}\sum_{i=1}^{N}\left|\frac{E_i - C_i}{E_i}\right| \times 100\% \tag{22}$$

where N represent the number of data, E_i and C_i are the experimental and calculated data, $\bar{E}$ and $\bar{C}$ represent the averages of E_i and C_i.

The correlation between the computed data and the experimental values from Fig. 1 (a) is revealed in Fig. 10 (a)-(c), respectively. Fig. 10 (a) shows *RMSE*, *R*, and *AARE* of true stress are 3.074, 0.998 and 2.468%, respectively. Fig. 10 (b) gives the correlation of AGS. *RMSE*, *R*, and *AARE* are determined as 2.583, 0.987 and 7.810%, respectively. Fig. 10 (c) illustrates the correlation of DRX fractions. *RMSE*, *R*, and *AARE* are calculated as 3.939, 0.992 and 8.956%, respectively. Furthermore, the scatter distributions of true stress, AGS and DRX fraction in Fig. 10 are close to the theoretical best fitting lines. Therefore, the true stress and microstructural evolution of Inconel 740 superalloy are well presented by the developed unified constitutive model.

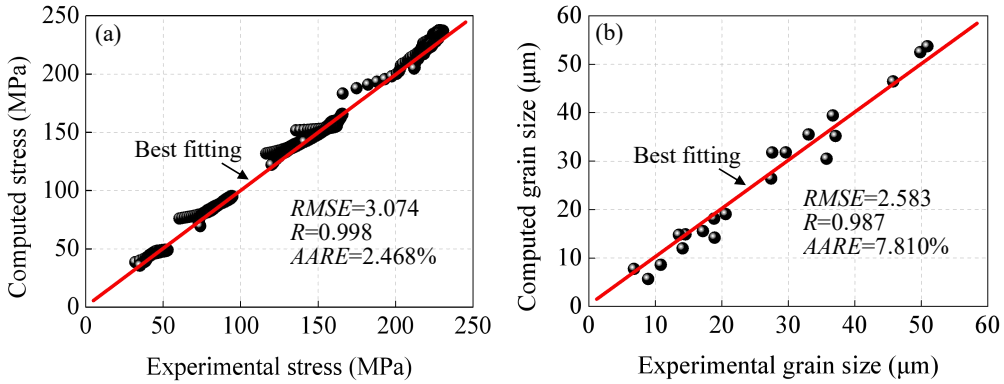

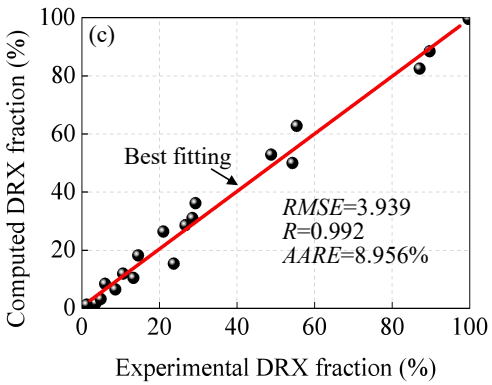

Fig.10. Correlation of the calculated and experimental results: (a) true stress, (b) AGS and (c) DRX fraction.

For further verifying the ability of the proposed constitutive model to predict the flow behavior of Inconel 740 superalloy under the deformation conditions outside the calibrated scope of this model, the predicted and experimental results of strain hardening rate ($\theta=d\sigma/d\varepsilon$) curve against the applied true strain at 1.0 s^{-1} and 1000 ˚C are represented by the solid curves and symbols, respectively, and are indicated in Fig. 11. The predicted true stress is close to the experimental results. Moreover, the positive θ value is dropped quickly when the deformation begins, indicating the dominance of hardening behavior. When θ value is zero, the peak stress and strain are reached on the corresponding true stress-strain curve [57]. With the further increase of strain, the dynamic softening mechanism dominated by DRX plays an active role when θ value becomes negative. The experimental and predicted θ values are always negative, while the two θ values at the strain of 0.8 are approaching zero. This shows that the experimental and predicted stress at 1000 ˚C and 1.0 s^{-1} will reach a steady state under a larger strain.

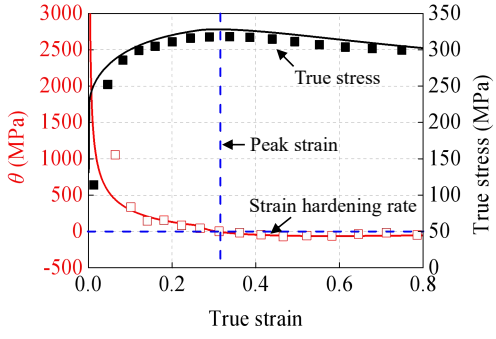

Fig.11. Comparison between the experimental (symbols) and computed (solid curves) curves of strain hardening rate and true stress for Inconel 740 superalloy obtained at 1000 ˚C and 1.0 s^{-1}.

5.2. The transient deformation tests and model validation

The applicability of the transient deformation caused by the instantaneous variation of strain rate for the developed unified constitutive model is analyzed. The two cases involved in Fig. 1 (b) are employed to verify this model. Fig. 12 (a) presents the microstructures of case I with the true strain of 0.51 and 0.8. The microstructure with the strain of 0.51 shows the typical necklace-like structures at the original grain boundaries and DRX grains within the initial grains. Similarly, the new grains indicated by the arrows are generated by the progressive subgrain rotation. The microstructure of the true strain of 0.8 is composed of the dominant DRX grains and some initial deformed grains. Moreover, Fig. 12 (b) illustrates the microstructures of case II at the true strain of 0.51 and 0.8. Similarly, the necklace-like structures and the new grains of original grain interiors are also apparent in the microstructure with the strain of 0.51. When the strain is 0.8, the coarse initial grains almost disappear and the microstructure consists of DRX grains. Furthermore, the decreasing strain rate can increase both the fraction and size of DRX grains at the large strain when the transient deformation happens at the medium strain from the comparison of Fig. 12 (a) and (b). One of the reasons is that the increased deformation time provided by the decreasing strain rate after the transient deformation promotes the development of DRX grains [58]. The other one is that the greater strain rate before the transient deformation generates the higher dislocation density, resulting in the more DRX grain nuclei used for the lower strain rate after the transient deformation [59].

Fig. 12 (c)-(e) present the predictive (solid curves) curves involving the flow stress, AGS, and DRX fraction and their experimental (symbols) results. The dashed curves extended from the predicted curves indicate the trend of stress, AGS and DRX fraction at the constant rate before the transient deformation. Fig. 12 (c) shows that the predictive flow stress in case I is increased again and the secondary hardening

stage appears after the transient deformation. The dislocation density accumulation from the low strain rate is not sufficient for achieving the critical dislocation density of DRX initiation under high strain rate, leading to the secondary hardening after the transient deformation. Subsequently, the true stress is gradually decreased due to the appearance of DRX. However, the computed true stress obtained at the constant rate of 0.1 s^{-1} is greater than the predictive curve in case I at the large strain. The dislocation stored from the low strain rate before the transient deformation makes a contribution to the DRX occurrence at the high strain rate. It is the reason why σ_c at the constant rate of 0.1 s^{-1} is greater than that after the transient deformation in case I. The detail of model corresponding to this phenomenon is reflected by Eq. (7). The experimental stress of case I at the large strain in Fig. 12 (c) is also lower than that of the constant rate of 0.1 s^{-1} in Fig. 8 (a). Furthermore, the predictive stress of case II after the transient deformation is rapidly declined and immediately dominated by the dynamic softening. The stored enough dislocation at the high strain rate before the transient deformation contributes to achieving the immediate occurrence of DRX behavior at the low strain rate [60]. The predicted stress curve of case II after the transient deformation is almost the same as the calculated stress at the constant rate of 0.01 s^{-1}. Furthermore, Fig. 12 (d) demonstrates that the calculated AGS curves at the constant rate of 0.1 and 0.01 s^{-1} are nearly coincident with the predictive curves in cases I and II at the large strain, respectively. The predictive AGS curve in case II at the large strain reaches steady state. From Fig. 12 (e), it is appeared that the predictive DRX fraction curve in case I at the strain of 0.8 is greater than the calculated curve of the constant rate of 0.1 s^{-1}, while this predictive curve in case II at the strain of 0.8 is slightly lower than the calculated curve of the constant rate of 0.01 s^{-1}. Through comparing two cases I and II during hot deformation, the falling strain rate is more favorable to increasing the fraction and size of DRX grains, which corresponds to the microstructures in Fig. 12 (a) and (b). Furthermore, the true stress, AGS and DRX fraction involved in the obtained experimental results can agree well with the corresponding predicted curves, as illustrated in Fig. 12 (c)-(e).

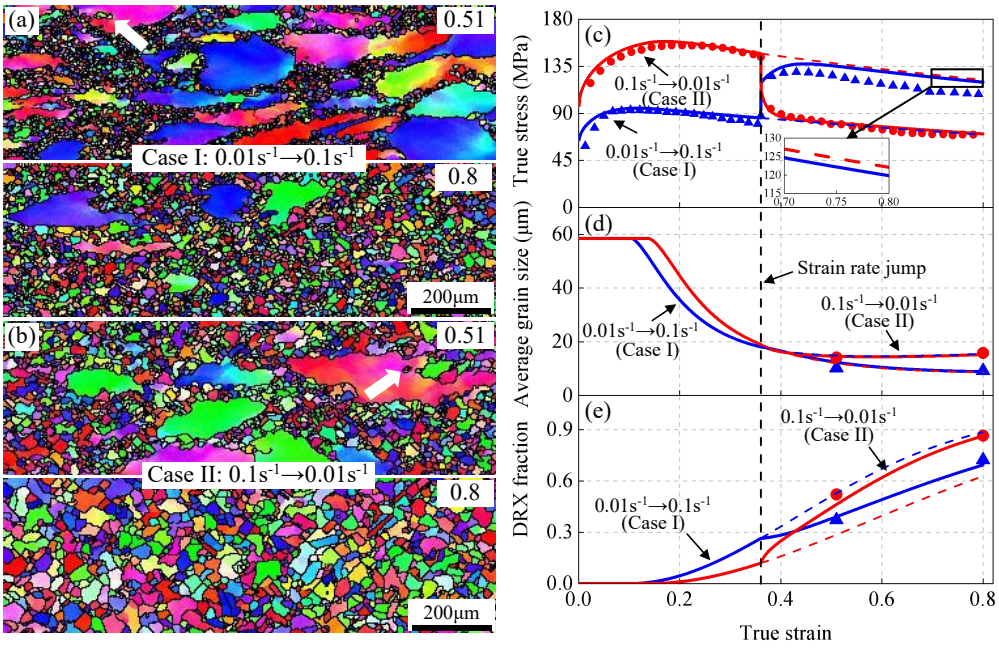

Fig.12. Validation of the unified constitutive model under 1100 ˚C and strain rate jump conditions: (a) the microstructures of the true strain of 0.51 and 0.8 in case I, and (b) the microstructures of the true strain of 0.51 and 0.8 in case II, comparison of the predictive and experimental data for the variation of (c) true stress, (d) AGS and (e) DRX fraction with the true strain, respectively. (The solid curves, symbols and dashed curves in (c)-(e) represent the predictive data, the experimental measurements and the calculated data at the constant strain rate, respectively).

5.3. Dynamic recrystallization diagram

As shown in Figs. 13 and 14, the DRX diagram predicted by the proposed constitutive model, including the dislocation density, DRX fraction and AGS, is developed for visualizing the DRX kinetics of Inconel 740 superalloy. The variations of normalized dislocation density, DRX fraction and AGS at the strain rate of 0.1 s^{-1}, true strain from 0 to1.0 and deformation temperature from 1080 to 1200 ˚C are displayed in Fig. 13 (a)-(c), respectively. The selective deformation temperatures are in the optimum temperature range for the workability of this superalloy [22]. Due to the dislocation multiplication caused by strain hardening, the dislocation density in Fig. 13 (a) is sharply increased at the beginning of deformation. The rising trend of the curve slows down when DRV happens and the critical dislocation density of DRX

initiation is reached. The dynamic softening mechanism dominated by DRX results in the dislocation annihilation after the peak dislocation density, and thus the dislocation density is reduced. Moreover, as the deformation temperature is increased, the dislocation density is gradually decreased. Furthermore, Fig. 13 (b) and (c) illustrate that the DRX fraction and AGS can be increased with temperature. Meanwhile, the ε_c value is reduced with increasing deformation temperature.

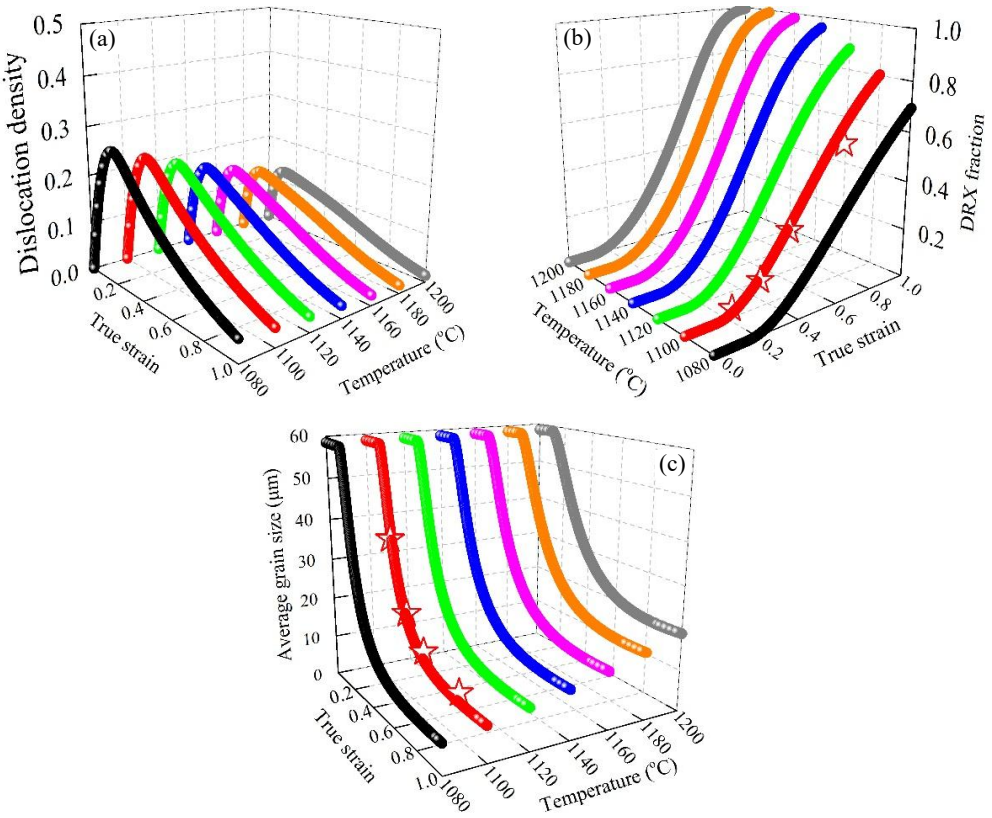

Fig.13. DRX diagram of Inconel 740 superalloy at 0.1 s^{-1} and different deformation temperatures described by (a) normalized dislocation density, (b) DRX fraction and (c) AGS. (Symbols ☆ represent the experimental results).

Fig. 14 (a)-(c) show the variations of dislocation density, DRX fraction and AGS at the deformation temperature of 1140 ˚C, true strain from 0 to1.0 and strain rate from 0.01 to 5.0 s^{-1}, respectively. Fig. 14 (a) reveals that the variation characteristics of single dislocation density curve are similar to that in Fig. 13 (a). The dislocation density amplitude is very small at 0.01s^{-1}. The dislocation density is increased with

strain rate. Moreover, with the increase of strain rate, Fig. 14 (b) shows the decrease of DRX fraction. From Fig. 14 (c), AGS at the large strain is inversely proportional to strain rate due to the small DRX grain size resulting from the high strain rate. However, AGS is increased as the strain rate exceeds 1.0 s^{-1}. This is because the DRX fraction in Fig. 14 (b) is much lower at 5.0 s^{-1}. In physics, Figs. 13 and 14 indicate that the longer time exposure of Inconel 740 superalloy deformed at high temperature encourages the occurrence of DRX at lower dislocation density.

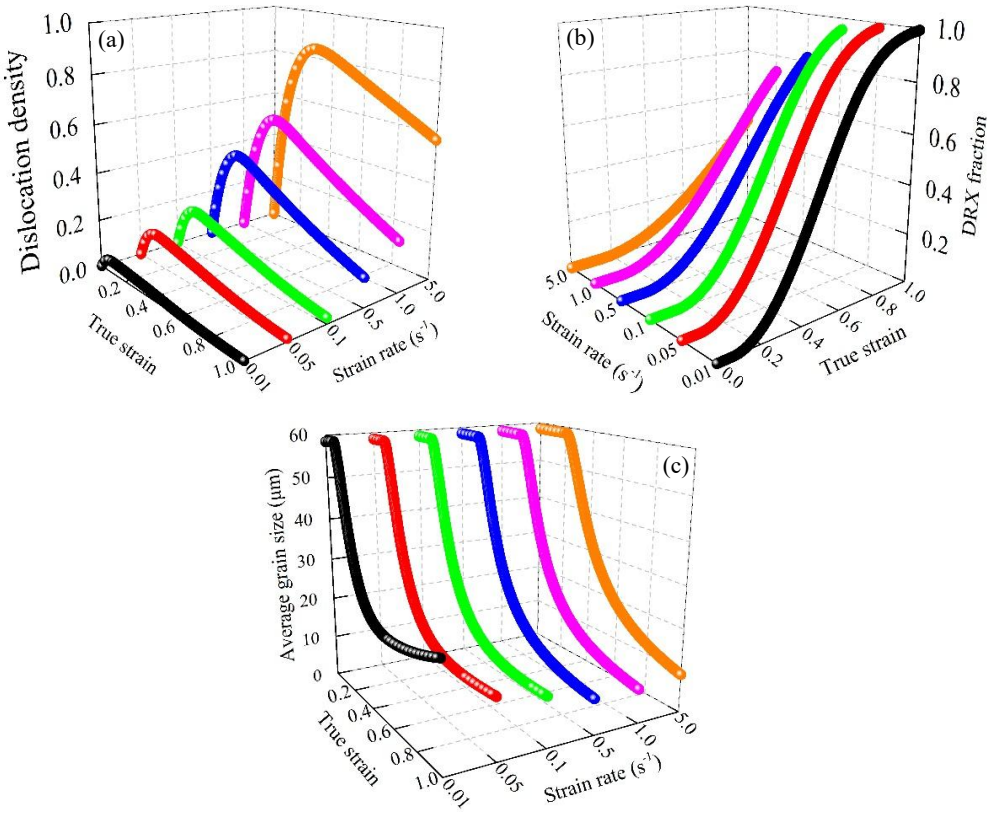

Fig.14. DRX diagram of Inconel 740 superalloy at 1140 ˚C and different strain rates described by (a) normalized dislocation density, (b) DRX fraction and (c) AGS.

6. Conclusions

The unified constitutive model involving the flow behavior and the microstructural evolution is developed for modelling the DRX behavior during hot deformation of Inconel 740 superalloy via the isothermal compression tests. The primary conclusions in this work are drawn as follows:

(1) By introducing the critical strain of DRX initiation, nucleation rate of DRX

grain and DRX grain size, a unified constitutive model applied to predict DRX behavior is proposed by for describing the variations of flow stress, AGS and DRX volume fraction and reflecting their physical evolution mechanism during hot deformation. Moreover, the flow stress at high strain rate and the strain hardening rate are also well predicted under the deformation conditions outside the calibrated scope of this model.

(2) Compared with the instantaneous increase of strain rate during hot deformation, the instantaneous decrease of strain rate increases the AGS and DRX fraction. The true stress after the instantaneous increase of strain rate is less than that at the corresponding to constant high strain rate. These complex hot deformation behaviors in the transient deformation process caused by the sudden change of strain rate are well predicted by the model.

(3) Based on this model, the DRX diagram in the optimal hot-workability temperature range is obtained to visualize the DRX kinetics involving the variation trends of dislocation density, DRX fraction and AGS. The prolonged exposure at high deformation temperature is beneficial to the occurrence of DRX at low dislocation density

Acknowledgements

Authors acknowledge the funding supported by NSAF (No. U1730121), National Defense Science and Technology Key Laboratory Fund Project (No. 6142902180201), National Natural Science Foundation of China (No. 51575039), Joint Foundation (general) project of the Ministry of Education (No. 6141A020221) and Fundamental Research Funds for the Central Universities (No. FRF-BD-19-003A, FRF-BD-18-003A and FRF-GF-19-003A).

Data Availability

The raw/processed data required to reproduce these findings cannot be shared at this time as the data also forms part of an ongoing study.

References

[1] R. Viswanathan, J.F. Henry, J. Tanzosh, G. Stanko, J. Shingledecker, B. Vitalis, R.

Purgert, U. S. program on materials technology for ultra-supercritical coal power plants, J. Mater. Eng. Perform. 14 (2005) 281-292.

[2] N.N. Aung, X. Liu, Effect of temperature on coal ash hot corrosion resistance of Inconel 740 superalloy, Corros. Sci. 82 (2014) 227-238.

[3] J.P. Shingledecker, N.D. Evans, G.M. Pharr, Influences of composition and grain size on creep-rupture behavior of Inconel® alloy 740, Mater. Sci. Eng. A 578 (2013) 277-286.

[4] N.D. Evans, P.J. Maziasz, R.W. Swindeman, G.D. Smith, Microstructure and phase stability in INCONEL alloy 740 during creep, Scripta Mater. 51 (2004) 503-507.

[5] G.S. Shin, J.Y. Yun, M.C. Park, S.J. Kim, Effect of Mo on the thermal stability of γ′ precipitate in Inconel 740 alloy, Mater. Charact. 95 (2014) 180-186.

[6] M. Abbasi, D.I. Kim, J.H. Shim, W.S. Jung, Effects of alloyed aluminum and titanium on the oxidation behavior of INCONEL 740 superalloy, J. Alloys Compd. 658 (2016) 210-221.

[7] T. Sakai, J.J. Jonas, Plastic Deformation: Role of Recovery and Recrystallization, Reference Module in Materials Science and Materials Engineering, Elsevier, Oxford, 2016.

[8] M.J. Wang, C.Y. Sun, M.W. Fu, Z.L. Liu, L.Y. Qian, Study on the dynamic recrystallization mechanisms of Inconel 740 superalloy during hot deformation, J. Alloys Compd. 820 (2020) 153325.

[9] Z.P. Hao, F.F. Ji, Y.H. Fan, J.Q. Lin, X.Y. Liu, S. Gao, Flow characteristics and constitutive equations of flow stress in high speed cutting Alloy 718, J. Alloys Compd. 728 (2017) 854-862.

[10] R.J. Immanuel, S.K. Panigrahi, Deformation behavior of ultrafine grained A356 material processed by cryorolling and development of Johnson-Cook model, Mater. Sci. Eng. A 712 (2018) 747-756.

[11] A. He, G. Xie, H. Zhang, X. Wang, A modified Zerilli-Armstrong constitutive model to predict hot deformation behavior of 20CrMo alloy steel, Mater. Des. 56 (2014) 122-127.

[12] H. Jiang, J. Dong, M. Zhang, Z. Yao, Phenomenological model for the effect of strain rate on recrystallization and grain growth kinetics in the 617B alloy, J. Alloys Compd. 735 (2018) 1520-1535.

[13] N. Haghdadi, D. Martin, P. Hodgson, Physically-based constitutive modelling of hot deformation behavior in a LDX 2101 duplex stainless steel, Mater. Des. 106 (2016) 420-427.

[14] V. Vilamosa, A.H. Clausen, T. Børvik, B. Holmedal, O.S. Hopperstad, A physically-based constitutive model applied to AA6082 aluminium alloy at large strains, high strain rates and elevated temperatures, Mater. Des. 103 (2016) 391-405.

[15] Y.C. Lin, X.M. Chen, D.X. Wen, M.S. Chen, A physically-based constitutive model for a typical nickel-based superalloy, Comp. Mater. Sci. 83 (2014) 282-289.

[16] H. Wei, G. Liu, M. Zhang, Physically based constitutive analysis to predict flow stress of medium carbon and vanadium microalloyed steels, Mater. Sci. Eng. A 602 (2014) 127-133.

[17] J. Lin, Y. Liu, A set of unified constitutive equations for modelling microstructure evolution in hot deformation, J. Mater. Process. Tech. 143-144 (2003) 281-285.

[18] H. Ji, J. Liu, B. Wang, X. Tang, J. Lin, Y. Huo, Microstructure evolution and constitutive equations for the high-temperature deformation of 5Cr21Mn9Ni4N heat-resistant steel, J. Alloys Compd. 693 (2017) 674-687.

[19] Z.X. Su, C.Y. Sun, M.W. Fu, L.Y. Qian, Physical-based constitutive model considering the microstructure evolution during hot working of AZ80 magnesium alloy, Adv. Manuf., 7 (2019) 30-41.

[20] W. Xiao, B. Wang, Y. Wu, X. Yang, Constitutive modeling of flow behavior and microstructure evolution of AA7075 in hot tensile deformation, Mater. Sci. Eng. A 712 (2018) 704-713.

[21] J. Lin, Y. Liu, D.C.J. Farrugia, M. Zhou, Development of dislocation-based unified material model for simulating microstructure evolution in multipass hot rolling, Philos. Mag. 85 (2005) 1967-1987.

[22] M. Wang, W. Wang, Z. Liu, C. Sun, L. Qian, Hot workability intergrating processing and activation energy maps of Inconel 740 superalloy, Mater. Today Commun. 14 (2018) 188-198.

[23] L. Tan, Y. Li, F. Liu, Y. Nie, L. Jiang, Microstructure evolutions of a powder metallurgy superalloy during high-strain-rate deformation, J. Alloys Compd. 789 (2019) 506-517.

[24] T. Konkova, S. Rahimi, S. Mironov, T.N. Baker, Effect of strain level on the evolution of microstructure in a recently developed AD730 nickel based superalloy during hot forging, Mater. Charact. 139 (2018) 437-445.

[25] Q. Zeng, B. Luan, Y. Wang, X. Zhang, R. Liu, K.L. Murty, Q. Liu, Effect of initial orientation on dynamic recrystallization of a zirconium alloy during hot deformation, Mater. Charact. 145 (2018) 444-453.

[26] T. Garcin, J.H. Schmitt, M. Militzer, In-situ laser ultrasonic grain size measurement in superalloy INCONEL 718, J. Alloys Compd. 670 (2016) 329-336.

[27] Y. Liu, Z. Yao, Y. Ning, Y. Nan, Effect of deformation temperature and strain rate on dynamic recrystallized grain size of a powder metallurgical nickel-based superalloy, J. Alloys Compd. 691 (2017) 554-563.

[28] H. Zhang, K. Zhang, H. Zhou, Z. Lu, C. Zhao, X. Yang, Effect of strain rate on microstructure evolution of a nickel-based superalloy during hot deformation, Mater. Des. 80 (2015) 51-62.

[29] Y.C. Lin, X.Y. Wu, X.M. Chen, J. Chen, D.X. Wen, J.L. Zhang, L.T. Li, EBSD study of a hot deformed nickel-based superalloy, J. Alloys Compd. 640 (2015) 101-113.

[30] Y. Wu, M. Zhang, X. Xie, F. Lin, S. Zhao, Dynamic recrystallization of a new nickel-based alloy for 700 °C A-USC power plant applications with different initial states: as-homogenized and as-forged, Mater. Sci. Eng. A 662 (2016) 283-295.

[31] K. Huang, R.E. Logé, A review of dynamic recrystallization phenomena in metallic materials, Mater. Des. 111 (2016) 548-574.

[32] Y. Liu, Y. Ning, Z. Yao, H. Li, X. Miao, Y. Li, Z. Zhao, Plastic deformation and dynamic recrystallization of a powder metallurgical nickel-based superalloy, J. Alloys Compd. 675 (2016) 73-80.

[33] N.R. Jaladurgam, A.K. Kanjarla, Hot deformation characteristics and microstructure evolution of Hastelloy C-276, Mater. Sci. Eng. A 712 (2018) 240-254.

[34] M. Zouari, N. Bozzolo, R.E. Loge, Mean field modelling of dynamic and post-dynamic recrystallization during hot deformation of Inconel 718 in the absence of δ phase particles, Mater. Sci. Eng. A 655 (2016) 408-424.

[35] L. Yang, B. Wang, G. Liu, H. Zhao, W. Xiao, Behavior and modeling of flow softening and ductile damage evolution in hot forming of TA15 alloy sheets, Mater. Des. 85 (2015) 135-148.

[36] J. Lin, T.A. Dean, Modelling of microstructure evolution in hot forming using unified constitutive equations, J. Mater. Process. Technol. 167 (2005) 354-362.

[37] O. EI Fakir, L. Wang, D. Balint, J.P. Dear, J. Lin, T.A. Dean, Numerical study of the solution heat treatment, forming, and in-die quenching (HFQ) process on AA5754, Int. J. Mach. Tools. Manuf. 87 (2014) 39-48.

[38] H. Li, J. Lin, T.A. Dean, S.W. Wen, A.C. Bannister, Modelling mechanical property recovery of a linepipe steel in annealing process, Int. J. Plast. 25 (2009) 1049-1065.

[39] M.S. Mohamed, A.D. Foster, J. Lin, D.S. Balint, T.A. Dean, Investigation of deformation and failure features in hot stamping of AA6082: Experimentation and modelling, Int. J. Mach. Tools. Manuf. 53 (2012) 27-38.

[40] N.D. Ryan, H.J. McQueen, Flow stress, dynamic restoration, strain hardening and ductility in hot working of 316 steel, J. Mater. Process. Technol. 21 (1990) 177-199.

[41] M. Bambach, I. Sizova, F. Silze, M. Schnick, Hot workability and microstructure evolution of the nickel-based superalloy Inconel 718 produced by laser metal deposition, J. Alloys Compd. 740 (2018) 278-287.

[42] C. Zhang, L. Zhang, W. Shen, C. Liu, Y. Xia, R. Li, Study on constitutive

modeling and processing maps for hotdeformation of medium carbon Cr-Ni-Mo alloyed steel, Mater. Des. 90 (2016) 804-814.

[43] R. Ding, Z.X. Guo, Coupled quantitative simulation of microstructural evolution and plastic flow during dynamic recrystallization, Acta Mater. 49 (2001) 3163-3175.

[44] R. Ding, Z.X. Guo, Microstructural modelling of dynamic recrystallisation using an extended cellular automaton approach, Comp. Mater. Sci. 23 (2002) 209-218.

[45] Y. Cai, C.Y. Sun, Y.L. Li, S.Y. Hu, N.Y. Zhu, E.I. Barker, L.Y. Qian, Phase field modeling of discontinuous dynamic recrystallization in hot deformation of magnesium alloys, Int. J. Plast. 133 (2020) 102773.

[46] H.E. Cho, Y. Hammi, A.L. Bowman, S. Karato, J.R. Baumgardner, M.F. Horstemeyer, A unified static and dynamic recrystallization Internal State Variable (ISV) constitutive model coupled with grain size evolution for metals and mineral aggregates, Int. J. Plast. 112 (2019) 123-157.

[47] C. Roucoules, M. Pietrzyk, P.D. Hodgson, Analysis of work hardening and recrystallization during the hot working of steel using a statistically based internal variable model, Mater. Sci. Eng. A 339 (2003) 1-9.

[48] G.R. Ebrahimi, A.R. Maldar, R. Ebrahimi, A. Davoodi, Effect of thermomechanical parameters on dynamically recrystallized grain size of AZ91 magnesium alloy, J. Alloys Compd. 509 (2011) 2703-2708.

[49] J. Cao, J. Lin, A study on formulation of objective functions for determining material models, Int. J. Mech. Sci. 50 (2008) 193-204.

[50] J. Lin, J. Yang, GA-based multiple objective optimisation for determining viscoplastic constitutive equations for superplastic alloys, Int. J. Plast. 15 (11) (1999) 1181-1196.

[51] R.P. Garrett, J. Lin, T.A. Dean, An investigation of the effects of solution heat treatment on mechanical properties for AA 6xxx alloys: experimentation and modelling, Int. J. Plast. 21 (2005) 1640-1657.

[52] A. Manonukul, F.P.E. Dunne, Initiation of dynamic recrystallization under inhomogeneous stress states in pure copper, Acta Mater. 47 (1999) 4339-4354.

[53] D.G. Cram, H.S. Zurob, Y.J.M. Brechet, C.R. Hutchinson, Modelling discontinuous dynamic recrystallization using a physically based model for nucleation, Acta Mater. 57 (2009) 5218-5228.

[54] A. Pougis, L.S. Toth, J.J. Fundenberger, A. Borbely, Extension of the Derby relation to metals severely deformed to their steady-state ultrafine-grain size, Scripta Mater. 72-73 (2014) 59-62.

[55] A. Nicolaÿ, G. Fiorucci, J.M. Franchet, J. Cormier, N. Bozzolo, Influence of strain rate on subsolvus dynamic and post-dynamic recrystallization kinetics of Inconel 718, Acta Mater. 174 (2019) 406-417.

[56] J. Fausty, N. Bozzolo, D.P. Muñoz, M. Bernachi, A novel level-set finite element formulation for grain growth with heterogeneous grain boundary energies, Mater. Des. 160 (2018) 578-590.

[57] H. Mirzadeh, A. Najafizadeh, The rate of dynamic recrystallization in 17-4 PH stainless steel, Mater. Des. 31 (2010) 4577-4583.

[58] D.G. He, Y.C. Lin, J. Chen, D.D. Chen, J. Huang, Y. Tang, M.S. Chen, Microstructural evolution and support vector regression model for an aged Ni-based superalloy during two-stage hot forming with stepped strain rates, Mater. Des. 154 (2018) 51-62.

[59] K.K. Li, M.S. Chen, Y.C. Lin, W.Q. Yuan, Microstructural evolution of an aged Ni-based superalloy under two-stage hot compression with different strain rates, Mater. Des. 111 (2016) 344-352.

[60] X. Tang, B. Wang, Y. Huo, W. Ma, J. Zhou, H. Ji, X. Fu, Unified modeling of flow behavior and microstructure evolution in hot forming of a Ni-based superalloy, Mater. Sci. Eng. A 662 (2016) 54-64.

Figure captions

Fig.1. Schematic of isothermal compression tests of Inconel 740 superalloy: (a) constant strain rate and (b) two cases of the transient deformation.

Fig.2. The initial state of Inconel 740 superalloy: (a) microstructure and (b) grain size distribution.

Fig.3. The microstructure of Inconel 740 superalloy obtained at the true strain of 0.36 and 1100 ˚C with a strain rate of (a) 0.01 s^{-1}, (b) 0.1 s^{-1} and (c) 1.0 s^{-1}.

Fig.4. The microstructure of Inconel 740 superalloy obtained at the strain of 0.51 and 0.01 s^{-1} with a deformation temperature of (a) 1000 ˚C, (b) 1100 ˚C and (c) 1200 ˚C.

Fig.5. The microstructure of Inconel 740 superalloy obtained at 0.01 s^{-1} and 1200 ˚C with a true strain of (a) 0.22, (b) 0.36 and (c) 0.8.

Fig.6. The critical strain of Inconel 740 superalloy: (a) the ε_c values and the example of determination of σ_c value and (b) the relationship between ε_c value and Z parameter.

Fig.7. The DRX grain size of Inconel 740 superallly: (a) the d_d values and (b) the relationship between d_d and Z parameter.

Fig.8. Comparison of calculated (solid curves) and experimental (symbols) true stress of Inconel 740 superalloy at (a) 1100 ˚C and (b) 0.01 s^{-1}.

Fig.9. Comparison between the calculated (solid curves) and experimental (symbols) data of Inconel 740 superalloy for (a) AGS, (b) DRX fraction at 1100 ˚C and different strain rates and (c) AGS, (d) DRX fraction at 0.01 s^{-1} and different deformation temperatures, respectively.

Fig.10. Correlation of the calculated and experimental results: (a) true stress, (b) AGS and (c) DRX fraction.

Fig.11. Comparison between the experimental (symbols) and computed (solid curves) curves of strain hardening rate and true stress for Inconel 740 superalloy obtained at 1000 ˚C and 1.0 s^{-1}.

Fig.12. Validation of the unified constitutive model under 1100 ˚C and strain rate jump conditions: (a) the microstructures of the true strain of 0.51 and 0.8 in case I, and (b) the microstructures of the true strain of 0.51 and 0.8 in case II, comparison of

the predictive and experimental data for the variation of (c) true stress, (d) AGS and (e) DRX fraction with the true strain, respectively. (The solid curves, symbols and dashed curves in (c)-(e) represent the predictive data, the experimental measurements and the calculated data at the constant strain rate, respectively).

Fig.13. DRX diagram of Inconel 740 superalloy at 0.1 s^{-1} and different deformation temperatures described by (a) normalized dislocation density, (b) DRX fraction and (c) AGS. (Symbols ☆ represent the experimental results).

Fig.14. DRX diagram of Inconel 740 superalloy at 1140 ˚C and different strain rates described by (a) normalized dislocation density, (b) DRX fraction and (c) AGS.

Table caption

Table 1. The material constant values in the unified constitutive model of Inconel 740 superalloy.